Effects of shear rate, confinement, and particle parameters on margination in blood flow

Marmar Mehrabadi, David N. Ku, and Cyrus K. Aidun*

George W. Woodruff School of Mechanical Engineering and Parker H. Petit Institute for Bioengineering and Bioscience, Georgia Institute of Technology, Atlanta, Georgia 30332, USA

(Received 1 February 2015; revised manuscript received 21 December 2015; published 16 February 2016)

The effects of flow and particle properties on margination of particles in red blood cell (RBC) suspensions is investigated using direct numerical simulation (DNS) of cellar blood flow. We focus on margination of particles in the flow of moderately dense suspensions of RBCs. We hypothesize that margination rate in nondilute suspensions is mainly driven by the RBC-enhanced diffusion of marginating particles in the RBC-filled region. We derive a scaling law for margination length in a straight channel. Margination length increases cubically with channel height and is independent of shear rate. We verify this scaling law for margination length by DNS of flowing RBCs and marginating particles. We also show that rigidity and size both lead to particle margination with rigidity having a more significant effect compared to size within the range of parameters in this study.

DOI: 10.1103/PhysRevE.93.023109

I. INTRODUCTION

When a dense suspension of uniformly distributed particles flows under confinement, the particle-particle and particle-wall interactions may lead to the development of a nonuniform concentration profile. Flow of binary suspensions under confinement may increase the concentration of one particle type at the wall. Mild segregation of particles can occur in binary suspensions of rigid spheres [1–4]. Segregation also occurs in liquid foams of bidisperse and polydisperse bubbles [5,6]. In suspensions of deformable particles, a high degree of segregation may occur and result in a severalfold increase in concentration of one particle type at the wall.

A physiologically relevant example of particle segregation in binary suspensions is margination of platelets in blood flow. Blood is a complex fluid consisting of 40% red blood cells (RBCs) by volume. Platelets are small blood cells (with a volume $\approx 10\ \mu m^3$) that form white clots to stop blood loss upon injury to arterial walls. Under arterial flow conditions, RBCs migrate away from the walls and platelets marginate to the RBC-free layer formed near the walls. Platelet margination increases the near-wall platelet concentration compared to the bulk platelet concentration [7–11]. This increased platelet concentration may contribute to the rapid formation of white clots, which is essential for preventing excessive blood loss. Platelet margination occurs in the presence of RBCs (i.e., above a threshold hematocrit of $\phi \approx 0.07$ [12]) and its rate increases with hematocrit [7,12–17] and RBC deformability [18–21]. In addition to platelets, leukocytes [22,23], stiff malaria-infected RBCs [24], and circulating cancer cells [25] may marginate under blood flow conditions.

Due to the particulate nature of margination, numerical investigation of this phenomenon requires a model that captures particle-particle and particle-fluid interactions. With advances in computer hardware and high performance computing, performing the direct numerical simulation (DNS) of the flow of suspensions of several hundred particles is possible [26,27]. Several recent studies have investigated the mechanism of margination in suspensions of deformable particles (for a recent review see [19]). Crowl and Fogelson [28] investigated platelet margination by performing two-dimensional simulations of flow of RBC and platelet suspension. They estimated platelet margination using a drift-diffusion equation similar to the approach of Eckstein and Belgacem [29]. With the drift and diffusion functions estimated from platelet trajectories, the drift-diffusion model underestimated the platelet margination rate by their cellular (DNS) blood flow simulations. To recover the results of the DNS cellular flow simulations, an additional drift term localized at the edge of the RBC-free was required. The authors hypothesized that the orientation angle of tank-treading RBCs at the edge of RBC-free layer may influence the motion of platelets at this region leading to a localized drift.

Numerical studies by Crowl and Fogelson [28] and Zhao *et al.* [30] suggest that, in contrast to blood flow in capillaries, volume exclusion due to RBC migration is insufficient for platelet margination in arterioles. Kumar and Graham [18,20] studied segregation by stiffness in dilute suspensions of deformable capsules and suggested that pair collisions between capsules of contrasting stiffness contribute to the segregation in such suspensions. In addition to stiffness, Kumar *et al.* [31] studied segregation by capsule size in suspensions of dilute and semidilute suspensions. To analyze their results, they used an idealized master equation that included the effect of heterogeneous collisions and migration velocity from wall. They found that in semidilute suspensions of capsules of differing deformability, segregation is due to both the differences in wall-induced migration velocity and heterogeneous collisions between such particles. In suspensions of unequal-sized capsules, segregation was mainly attributed to differences in wall-induced migration velocity. Both of these mechanisms may dominate particle migration across a large portion of the channel in semidilute suspensions flowing in relatively small channels; however, these mechanisms may only affect the dynamics in the near-wall region in the flow of dense suspensions in larger channels. Vahidkhah *et al.* [32] suggested that platelet margination is due to formation of local clusters and cavities in RBC distribution. They proposed that once platelets enter these cavities, they rapidly marginate towards the wall. Note that in [18,28,30] Poiseuille flow is considered; however, in [20,31,32] shear flow with a linear velocity profile

*cyrus.audin@me.gatech.edu

is considered. The flow configuration may affect margination behavior. For example, the magnitude and profile of particle migration velocity and the steady-state position of particles in Poiseuille flow differ from those in shear flow [33,34]. Also, note that [18,20,30,31] have assumed a Reynolds number of $\mathrm{Re} = 0$, while in [28,32] nonzero Re has been assumed. Although, the values of particle Reynolds number are small in the above studies, the inertia may still affect the results (see [33,35]).

In addition to investigating the mechanism of margination with model systems, numerical experiments using DNS can help identify important parameters that affect this process [36,37]. Identifying parameters affecting margination can help in the design and optimization of devices that employ margination for separation of particles and cells from blood, such as malaria-infected RBCs [24], leukocytes [38], and circulating cancer cells [25]. Furthermore, identifying particle properties that affect margination are important for the design of more effective vascular-targeted nanocarriers and microcarriers [39–43].

In this study we focus on margination of particles in the flow of moderately dense suspensions of RBCs flowing under strong to weak confinements. The wall-induced lift force on RBCs and marginating particles strongly depends on the properties of these particles, particularly their size and deformability. The difference in the wall-induced lift force results in faster migration of RBCs compared to marginating particles. In dilute and semidilute suspensions flowing under strong confinements (i.e., with a high ratio of particle size to the channel size), this difference in wall migration velocity may strongly affect margination rate. However, in the flow of moderately dense suspensions, RBC motions dominate the local hemodynamics in the RBC-laden region and could screen the effect of the wall on RBCs and marginating particles. Thus, we hypothesize that the margination rate is mainly driven by the RBC-enhanced diffusion of marginating particles in the RBC-laden region. Based on this hypothesis, we derive a scaling law to identify important parameters affecting margination length L_D. We perform DNS of flowing RBCs and marginating particles to verify our proposed scaling law for margination length. Also, to investigate the margination mechanism, we identify those properties of platelets that lead to their margination in blood flow. In particular, we investigate whether platelets marginate because of their smaller size or less deformability compared to RBCs. We also investigate the effect of the shape of marginating particles on margination rate.

II. SCALING RELATION FOR MARGINATION LENGTH

To obtain a scaling relation for margination length in a suspension of RBCs and marginating particles, we follow the analysis of Nott and Brady [44], who estimated the development length of concentration profiles in suspensions of rigid spheres. The scaling analysis is based on the hypothesis that shear-induced diffusivity governs particle margination rate. Shear-induced diffusion coefficient in a monodispersed suspension of particles scales as

$$D_{yy} = K\dot{\gamma}a^2, \tag{1}$$

where D_{yy} is the shear-induced diffusion coefficient in the lateral direction y, $\dot{\gamma}$ is the shear rate, a is the particle radius, and K is a nondimensional constant [45–47]. In suspensions of rigid spheres, K is a function of suspension volume fraction ϕ. In the binary suspensions of RBCs and marginating particles considered here, marginating particles often interact with RBCs because of their lower volume fraction compared to RBCs. Therefore, we use the term RBC-enhanced shear-induced diffusion (RESID) to describe the diffusion of marginating particles due to hydrodynamic effects. The value of the diffusion constant K for the RESID coefficient depends on the RBC volume fraction ϕ and both RBC and marginating particle properties such as particle deformability and shape.

Assuming that RESID governs lateral displacement of particles in the RBC-filled region, we can derive an expression for the margination length scale

$$L_D \sim \frac{H^3}{12Ka^2} \tag{2}$$

in a suspension of RBCs and marginating particles flowing between two parallel plates with a separation distance of H (see the Appendix for a simple derivation). From this scaling relation, the margination length L_D scales cubically with channel height H and is not an explicit function of the shear rate $\dot{\gamma}$. Margination length depends on $\dot{\gamma}$ only through the weak change of K with $\dot{\gamma}$. In addition to H and $\dot{\gamma}$, (2) implies that the margination rate depends on the relative size of the marginating particles. We will test the validity of the above scaling law in Sec. IV.

III. METHODS

The suspensions of RBCs and marginating particles are directly simulated with a coupled lattice-Boltzmann–spectrin-link (LB-SL) method [36,48]. In the LB-SL method, a lattice-Boltzmann solver for the fluid phase (i.e., blood plasma and RBC cytoplasm) is coupled to a coarse-grained spectrin-link model for the RBC membranes and a rigid dynamic solver for the platelets. Reasor *et al.* developed the LB-SL method based on the initial hybrid lattice-Boltzmann–finite-element implementation of MacMeccan *et al.* [49]. The SL method for modeling the dynamics of the RBC membrane improves on the linear finite-element model of [49] by enabling simulation of larger deformations of RBC membrane at higher capillary numbers at no additional computational cost. In addition, the SL method captures tank-treading dynamics. The LB-SL solver is parallelized using the message interfacing protocol to enabled simulation of $O(10^5)$ particles [26].

The SL-LB method has been validated by a comparison of the mechanical response of individual RBCs with experiments and other computational approaches, such as the deformation of RBCs stretched by optical tweezers, the deformation of isolated RBCs under high shear, and the parachuting RBCs in Hagen-Poiseuille flow [48]. The numerical tests performed show good agreement with experimental results and the use of fewer computational resources compared to previous methods used for modeling suspensions. In addition, the SL-LB method has been validated for large-scale simulations performed to predict the rheological properties of blood in unbounded

shear conditions, showing good agreement with rotational viscometer results from the literature [50].

A. Lattice-Boltzmann method

The method used to solve for the fluid phase (i.e., blood plasma and RBC cytoplasm) is based on the D3Q19 single-relaxation-time LB implementation of Aidun *et al.* [51] and Ding and Aidun [52]. Using a Chapman-Enskog expansion (see, e.g., [53]), it can be shown that the LB equations converge to the Navier-Stokes equations. The LB method is favorable for simulating suspensions due to several factors. The computational expense of this method scales linearly with the number of particles since particle interactions are propagated on time scales below time scales of particle motions [54,55]. In addition, the time evolution of the fluid particle distribution at each node only requires the knowledge of particle distribution functions at neighboring nodes, making all calculations localized in space, which makes the LB method optimal for parallel computing. A detailed description of the LB method can be found in [53,56,57].

The LB method is a mesoscopic approach based on discretization of the Boltzmann equation in velocity space in terms of a chosen set of velocity vectors $\boldsymbol{e}_i$, where $i = 1,\ldots,Q$. This chosen velocity vector set results in a discrete lattice space denoted by $\boldsymbol{x}$. The particle distribution function f_i existing at each node can be thought of as the density of mesoscopic particles restricted to flow with velocities of $\boldsymbol{e}_i$. At each time step, the evolution of f_i is governed by the streaming and collision operators. Using the single-relaxation-time collision operator of Bhatnagar, Gross, and Krook [58], the time evolution of the particle distribution function can be written as

$$f_i(\boldsymbol{x}+\boldsymbol{e}_i,t+1) = f_i(\boldsymbol{x},t) - \frac{1}{\tau}[f_i(\boldsymbol{x},t) - f_i^{(\mathrm{eq})}(\boldsymbol{x},t)], \quad (3)$$

where τ is the Bhatnagar-Gross-Krook relaxation-time parameter determining the rate of relaxation to a local equilibrium distribution function $f_i^{(\mathrm{eq})}$. The macroscopic flow kinematic viscosity ν is related to the relaxation time by $\nu = c_s^2(\tau - 1/2)$, where c_s is the LB pseudo-sound-speed. At low Mach numbers, i.e., small u/c_s, the local equilibrium distribution can be approximated in terms of local macroscopic variables as

$$f_i^{(\mathrm{eq})}(\boldsymbol{x},t) = w_i\rho\left[1 + \frac{1}{c_s^2}(\boldsymbol{e}_i\cdot\boldsymbol{u}) + \frac{1}{2c_s^4}(\boldsymbol{e}_i\cdot\boldsymbol{u})^2 - \frac{1}{2c_s^2}(\boldsymbol{u}\cdot\boldsymbol{u})\right], \quad (4)$$

where ρ and $\boldsymbol{u}$ are the macroscopic density and velocity and w_i denotes lattice constants that depend on the LB stencil used. For the D3Q19 stencil used in this study, w_i is 1/3, 1/18, and 1/36 for the rest, nondiagonal, and diagonal directions, respectively. The LB pseudo-sound-speed is $c_s = \sqrt{1/3}$. By definition, the first and second momenta of the discrete distribution functions provide the macroscopic density $\rho(\boldsymbol{x},t) = \sum_i f_i(\boldsymbol{x},t)$ and momentum $\rho(\boldsymbol{x},t)\mathrm{u}(\boldsymbol{x},t) = \sum_i f_i(\boldsymbol{x},t)\mathrm{e}_i$.

B. Coarse-grained spectrin-link RBC membrane model

The SL model for deformable RBC membranes is inspired by the physiological construction of the RBC membrane itself, which consists of a cytoskeleton mainly formed by a network of spectrin proteins attached to the RBC membrane lipid bilayer. In the SL approach, the RBC membrane is modeled as a two-dimensional triangular network on the RBC surface. Modeling the RBC membrane using spectrin-link lengths of $\sim O(100\ \mathrm{nm})$, i.e., on the order of protein lengths in an actual RBC, requires more than 25 000 vertices per RBC triangulation [59,60]. Such a high resolution for modeling each RBC is impractical for simulation of blood flow with $O(10^3)$ RBCs. Using a coarse-grained SL approach developed by Pivkin and Karniadakis [61] and further improved by Fedosov *et al.* [62,63], the RBC membrane can be modeled by a much smaller number of nodes (250–300) while still accurately capturing the membrane elastic response at both small and large deformations.

In the SL model used in this study, the RBC membrane is modeled by a triangulated network. The vertices of the mesh located at $\{\boldsymbol{x}_i\}$, $i \in 1,\ldots,N_v$, are connected with N_s springs with lengths of l_i, $i \in 1,\ldots,N_s$, forming N_t triangles with areas of A_k, $k \in 1,\ldots,N_t$. The Helmholtz free energy of the spectrin network F includes in-plane energy $F_{\text{in-plane}}$, bending energy F_κ, volume conservation constraint F_V, and area conservation constraint F_A,

$$F(\{\boldsymbol{x}_i\}) = F_{\text{in-plane}} + F_\kappa + F_V + F_A. \quad (5)$$

The in-plane free energy $F_{\text{in-plane}}$ includes the contributions of elastic energy stored in spectrin proteins and hydrostatic elastic energy stored in the membrane

$$F_{\text{in-plane}} = \sum_{i\in 1\cdots N_s} U_{\mathrm{WLC}}(l_i) + \sum_{k\in 1\cdots N_t}\frac{C_q}{A_k^q}. \quad (6)$$

The first sum in (6) represents the elastic energy stored in spectrin links described in terms of the wormlike chain (WLC) model [64,65]

$$U_{\mathrm{WLC}}(l_i) = \frac{k_B T l_m}{4p}\frac{3x_i^2 - 2x_i^3}{1-x_i}, \quad (7)$$

where k_B is the Boltzmann constant, T is absolute temperature, p is the persistence length, and $x = l_i/l_m \in [0,1)$, where l_m is the maximum length of the spectrin links. The attractive potential from the WLC spring forces is balanced by a repulsive potential represented by the second sum in (6). This term represents the hydrostatic energy in stored in the membrane patches. The constant C_q can be derived by applying the virial theorem and setting the obtained Cauchy stress to zero [62,63,66],

$$C_q = \frac{\sqrt{3}A_{l_0}^{q+1}k_B T\left(4x_0^2 - 9x_0 + 6\right)}{4pql_m(1-x_0)^2}, \quad (8)$$

where $x_0 = l_0/l_m$, l_0 is the average length of the links at equilibrium, and $A_{l_0} = \sqrt{3}l_0^2/4$. We use $q = 1$ in this study.

The bending energy is defined as

$$F_\kappa = \sum_{j\in 1,\ldots,N_s}\tilde{\kappa}[1 - \cos(\theta_j - \theta_0)], \quad (9)$$

where $\tilde{\kappa}$ is the discrete bending constant, θ_j is the instantaneous angle between adjacent triangles sharing the link j, and θ_0 is the spontaneous angle. The discrete bending modulus $\tilde{\kappa}$ is related to the average bending modulus κ by $\tilde{\kappa} = 2\kappa/\sqrt{3}$ [63,67].

The volume conservation constraint is a nonphysical energy implemented to impose the incompressibility of RBC cytoplasm

$$F_V = \frac{k_v\left(V - V_0^t\right)^2}{2V_0^t}, \tag{10}$$

where V is the instantaneous volume of RBCs and V_0^t is the total desired volume of RBCs. Similarly, the area conservation constraint is a nonphysical energy implemented to account for the membrane inextensibility

$$F_A = \frac{k_a\left(A^t - A_0^t\right)^2}{2A_0^t}, \tag{11}$$

where A^t is the total instantaneous area of the membrane, $A^t = \sum_{i\in 1,\ldots,N_t} A_i$, and A_0^t is the desired membrane area.

The forces on the network vertices resulting from the above energies are derived by

$$\boldsymbol{f}_i^m = \frac{\partial F(\{\boldsymbol{x}_i\})}{\partial \boldsymbol{x}_i}. \tag{12}$$

The expressions for the force expressions can be derived analytically (see Appendix A of [66]).

The location of each vertex $\boldsymbol{x}_i$ is updated by applying the total force $\boldsymbol{f}_i^t$ on each vertex

$$\frac{d\boldsymbol{x}_i}{dt} = \boldsymbol{v}_i, \quad \boldsymbol{f}_i^t = \boldsymbol{f}_i^m + \boldsymbol{f}_i^{\mathrm{FS}} + \boldsymbol{f}_i^{\mathrm{PP}}, \tag{13}$$

where $\boldsymbol{f}_i^{\mathrm{FS}}$ is the force due to fluid-solid coupling and $\boldsymbol{f}_i^{\mathrm{PP}}$ is the force due to particle-particle interactions. The calculation of contact forces due to particle-particle interactions are discussed in detail by MacMeccan *et al.* [49] and Clausen *et al.* [68]. The locations of the vertices are updated via Newton's equations of motion using a first-order accurate forward Euler scheme.

C. Rigid particle model

Platelets are modeled as rigid particles. A triangular mesh represents the surface of rigid particles. To update the dynamics of rigid particles, the forces due to fluid-solid and particle-particle interactions are calculated on triangular elements and nodes on the surface of the particles. The total force on each rigid particle is calculated by summing the forces on the surface nodes

$$\boldsymbol{f}_p^t = \sum_{i\in 1,\ldots,N_v} \boldsymbol{f}_i^{\mathrm{FS}} + \boldsymbol{f}_i^{\mathrm{PP}}. \tag{14}$$

Similarly, the total torque on a rigid particle is calculated via

$$\boldsymbol{T}_p^t = \sum_{i\in 1,\ldots,N_v} (\boldsymbol{x}_p - \boldsymbol{x}_i) \times \left(\boldsymbol{f}_i^{\mathrm{FS}} + \boldsymbol{f}_i^{\mathrm{PP}}\right), \tag{15}$$

where $\boldsymbol{x}_p$ denotes the location of the center of mass of the particle. With the total force and torque on a rigid particle, the motion of the particle is solved via Newton's equations for translation

$$M\frac{d\boldsymbol{v}_p}{dt} = \boldsymbol{f}_p^t \tag{16}$$

and for rotation

$$\boldsymbol{I}\frac{d\boldsymbol{\Omega}_p}{dt} + \boldsymbol{\Omega}_p \times (\boldsymbol{I}\cdot\boldsymbol{\Omega}) = \boldsymbol{T}_p^t, \tag{17}$$

where M is the mass, $\boldsymbol{I}$ is the inertial tensor, $\boldsymbol{v}_p$ is the linear velocity, and $\boldsymbol{\Omega}_p$ is the angular velocity of the rigid particle. The density of rigid particles is assumed to be equal to the density of plasma, i.e., $\rho = 1$ g/cm^3, for calculating M and $\boldsymbol{I}$. The position and orientation of rigid particles at each time step are updated by solving (16) and (17) using a first-order accurate forward Euler scheme.

D. Fluid-solid coupling

The fluid-solid coupling is based on the bounceback method of Aidun *et al.* [51] and is described in detail by MacMeccan *et al.* [49] and Clausen *et al.* [68]. In this method, the momentum transfer at the fluid-solid interface is accounted for by applying the standard bounceback scheme along lattice links that cross solid surfaces. Using the bounceback method, the no-slip condition is enforced by adjusting the distributions of fluid nodes at the end points of a link in the i direction via

$$f_{i'}(\boldsymbol{x},t+1) = f_i(\boldsymbol{x},t^+) - 6\rho\omega_i\boldsymbol{u}_b\cdot\boldsymbol{e}_i, \tag{18}$$

where i' is the direction opposite to i, $f_i(\boldsymbol{x},t^+)$ is the postcollision distribution, and $\boldsymbol{u}_b$ is the solid velocity at the intersection point with the link. The fluid force on the solid surface is determined by

$$\boldsymbol{f}^{\mathrm{FS}}\left(\boldsymbol{x} + \tfrac{1}{2}\boldsymbol{e}_i, t\right) = 2\boldsymbol{e}_i[f_i(\boldsymbol{x},t^+) + 3\rho\omega_i\boldsymbol{u}_b\cdot\boldsymbol{e}_{i'}]. \tag{19}$$

E. Calculation of RBC-enhanced diffusion of platelets from DNS

The diffusivity of particles is estimated by analyzing single-particle trajectories from the DNS model. The shear-induced diffusivity can be estimated from mean square displacements of platelets as a function of time (see, e.g., [19,28,30,69]). Here we estimate the diffusion coefficient from step sizes and wait times between successive particle collisions from platelet trajectories. Calculating the step size of particle jumps $\Delta y(y)$ and wait times between successive jumps $\tau(y)$ from particle trajectories, the diffusivity in the y direction can be estimated as

$$D_{yy}(y) = \frac{\langle \delta y^2(y)\rangle}{2\langle\tau(y)\rangle}, \tag{20}$$

where $\langle \delta y^2(y)\rangle$ is the time average of the variance of the jump step sizes and $\langle\tau(y)\rangle$ is the time average of wait times τ. The calculated values of $\tau(y)$ and $\Delta y(y)$ depend on the time step Δt for resolving the particle trajectories. Resolving particle trajectories with a time step of the same order as the DNS time step resolves the actual fluctuations of the particles within the accuracy of the DNS model. If the time step for particle trajectories Δt is much larger than the actual wait times between jumps τ, then the estimated $\langle\tau(y)\rangle$ approaches the time step used for resolving the trajectories.

Therefore, if particle trajectories are resolved with relatively large time steps, calculating the diffusion coefficient from (20) is equivalent to calculating it from a linear growth of mean square lateral displacements of particles with time $\langle y^2(t)\rangle = 2t\,D_{yy}$. We used $\Delta t \sim 1/\dot{\gamma}$ for resolving particle trajectories.

F. Setup

We consider the flow of RBC and platelet suspensions between two parallel plates with distances of $H = 40$, 80, and 160 μm. The flow is driven by a constant body force in the axial direction x. The direction normal to the walls is denoted by y with walls located at $y = 0$ and $y = H$. Periodic boundary conditions are applied in the flow direction x and the z direction normal to both the x and y directions. A domain length of $L = 80$ μm was chosen for the channels of height $H = 40$ μm. For channels of height $H = 80$ and 160 μm, a domain length of $L = 40$ μm was chosen to lower computational cost. We investigated the effect of domain length L in the flow direction on RBC migration and platelet margination rates. A comparison of margination rates between domains of length $L = 40$ and 80 μm showed negligible differences for channels of height $H = 80$ and 160 μm. In all cases, the channel depth in the z direction was set to 40 μm.

The RBC membrane is resolved by a triangular mesh with 6×10^2 nodes. At equilibrium, the RBCs are biconcave shaped, 8 μm in diameter. The ratio of RBC cytoplasm to plasma viscosity is set to the physiological viscosity ratio of $\lambda = 5$. The density of RBC cytoplasm is assumed to be equal to the density of plasma, i.e., $\rho = 1$ g/cm^3. The mechanical properties of normal RBCs are set as follows: The RBC membrane bending modulus $\tilde{\kappa} = 4.7 \times 10^{-18}$ J, the RBC membrane shear modulus $G = 6.3 \times 10^{-6}$ J/m^2, the RBC area constraint coefficient $k_a = 1.7 \times 10^{-5}$ J/m^2, and the RBC volume constraint coefficient $k_v = 50.9$ J/m^3. The above values of G and λ lie within the range of experimentally measured values of RBC mechanical properties [70]. In the spectrin-link model, the volume and area constraints are applied to ensure cytoplasm incompressibility and membrane inextensibility and the exact values of k_v and k_a are unimportant [59,63]. The bending modulus is about an order of magnitude larger than the experimental consensus values for $\tilde{\kappa}$. This relatively large value for $\tilde{\kappa}$ is needed for stabilizing the biconcave shape of the RBCs at low shear rates [59].

The channel hematocrit, hereafter referred to as hematocrit, is defined by the volume fraction of RBCs in the channel at any instant of time. The hematocrit $\phi(y)$ as a function of distance in the cross flow direction y is calculated as the volume fraction of RBCs along the flow direction x at any point y. The average hematocrit value for a channel $\bar{\phi}$ represents $\bar{\phi} = \int_{y=0}^{y=H} \phi(y)dy/H$. The discharge hematocrit $\phi_d(y)$ is the RBC volume fraction in blood flowing out of a channel. Under physiological conditions, the value of the discharge hematocrit is close to the systemic hematocrit. Due to migration of RBCs to the channel center (Fåhræus effect), the average channel hematocrit in microchannels is smaller than the average discharge hematocrit $\bar{\phi}_d$. We set the average channel hematocrit $\bar{\phi} = 0.20$ in all simulations. The volume fraction of marginating particles (0.018–0.037) is chosen to be higher than physiological values for platelet volume fraction in blood (~0.002) to provide more samples for analysis of margination. To place RBCs and marginating particles, initially, a large number of particles was distributed in the domain with random locations and orientations. Marginating particles were selected from the pool of particles such that they were distributed evenly in the y direction (but not necessarily in the x and z directions). Red blood cells were randomly picked from the remaining pool of particles.

IV. RESULTS

In this section we report the effects of shear rate, channel size, particle size, and the deformability and particle aspect ratio on margination.

A. Effect of shear rate

We studied the effect of shear rate on platelet margination by simulating the flow of RBC and platelet suspensions in channels of height $H = 40$ μm and varying $\dot{\gamma}_w$ from 10^3 to 2×10^4 s^{-1}. From experimentally measured velocities in arterioles of diameter $D \approx 30$–80 μm, the wall shear rate in small arterioles can be estimated as $\dot{\gamma}_w \approx (2 \times 10^3)$–$(8 \times 10^3)$ [71–74].

The wall shear rates $\dot{\gamma}_w$ are based on matching channel Reynolds number $\mathrm{Re} = \rho\dot{\gamma}_w H^2/\mu$ and RBC shear capillary number $\mathrm{Ca}_G = a_{\mathrm{RBC}}\bar{\dot{\gamma}}\mu/G$, where ρ is the plasma density, μ is the plasma viscosity, G is the RBC membrane shear modulus, and a_{RBC} is the RBC effective radius [$a_{\mathrm{RBC}} = (0.75V_{\mathrm{RBC}}/\pi)^{1/3}$, with V_{RBC} the RBC volume]. The RBC Reynolds number is defined as $\mathrm{Re}_{\mathrm{RBC}} = \rho\bar{\dot{\gamma}}a_{\mathrm{RBC}}^2/\mu$. The simulation parameter details are given in Table I. The RBCs have an effective radius $a_{\mathrm{RBC}} = 2.9$ μm, resulting in a confinement ratio of $2a_{\mathrm{RBC}}/H = 0.145$. A total number of 240 RBCs results in $\phi = 0.20$. The platelets are modeled as rigid oblate spheroids with a major axis of 2.3 μm and aspect ratio of 2.3. A total number of 100 platelets is used in each simulation. The initial randomly distributed locations of RBCs and platelets are identical in all cases.

Figure 1 shows snapshots from simulations at $\dot{\gamma}_w = 10^3$ and 2×10^4 s^{-1} at an average traveled distance of $\bar{x} = 9$ mm (i.e., $\bar{x}/H = 225$). At both shear rates, a RBC-free layer forms at wall and platelets concentration increases in this region. At a higher shear rate of $\dot{\gamma}_w = 2 \times 10^4$ s^{-1}, RBCs are more stretched and elongated along the flow direction compared to $\dot{\gamma}_w = 1 \times 10^3$ s^{-1}. This larger deformation of RBCs and higher lift force from the wall at $\dot{\gamma}_w = 20 \times 10^3$ lead to a larger RBC-free layer δ compared to that at $\dot{\gamma}_w = 1 \times 10^3$. To quantify the effect of $\dot{\gamma}_w$ on δ, we defined δ from the RBC

TABLE I. DNS parameters of test cases for studying the effect of shear rate on margination. The domain size is $80 \times 40 \times 40$ μm^3 and the RBC volume fraction is $\phi = 0.20$.

Simulation	$\dot{\gamma}_w$ (s^{-1})	Ca_G	Re	$\mathrm{Re}_{\mathrm{RBC}}$
1	10^3	0.23	1.6	0.004
2	5×10^3	1.2	8	0.02
3	10^4	2.3	16	0.04
4	2×10^4	4.7	32	0.09

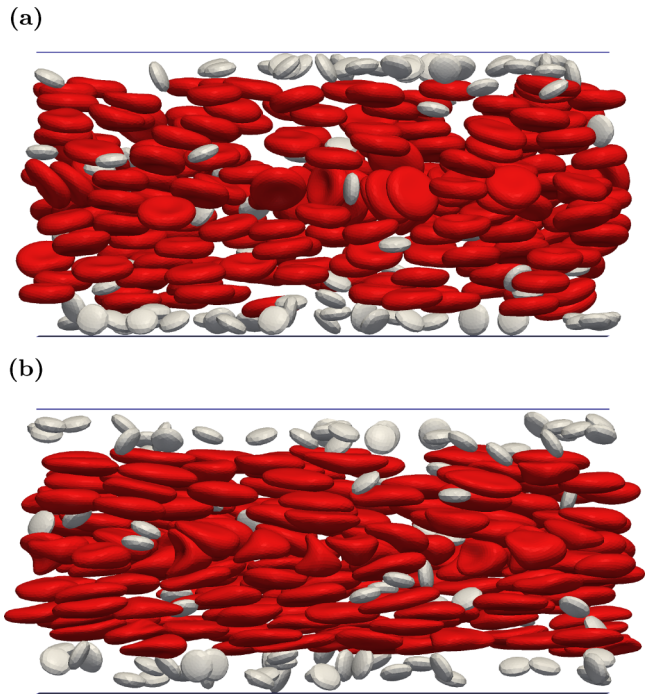

FIG. 1. Simulation snapshots of RBC and platelet suspensions flowing in channels of height $H = 40$ μm at shear rates of (a) $\dot{\gamma}_w = 1000$ s^{-1} and (b) $\dot{\gamma}_w = 20\,000$ s^{-1}.

hematocrit profiles after reaching equilibrium such that $\phi(\delta) = 0.005$ (Fig. 2). In channels of height $H = 40$ μm, we found $\delta = 3.0$, 3.8, 4.6, and 5.2 μm at wall shear rates of $\dot{\gamma}_w = 10^3$, 5×10^3, 10^4, and 2×10^4 s^{-1}, respectively. The RBC-free layer thickness follows a power-law relation of $\delta \propto \mathrm{Ca}_G^{0.2}$. *In vitro* experiments of Kameneva *et al.* [75] in 100-μm square channels showed that the δ of RBC suspensions with $\phi = 0.20$ follows a similar power-law trend over a range of shear rates of $\dot{\gamma}_w \sim (1.5 \times 10^3)$–$(7 \times 10^4)$ s^{-1}.

To quantify the effect of $\dot{\gamma}_w$ on margination length, we calculated the average relative distance of platelets from wall $\Delta\overline{w}(t) = \overline{w}(t) - \overline{w}(0)$, where $\overline{w}(t)$ denotes the average distance of marginating particles from the wall $\overline{w}(t) = H/2 - \overline{|y(t) - H/2|}$. Figure 3(a) shows $\Delta\overline{w}$ as a function of time for various $\dot{\gamma}_w$ values. The average distance of platelets from the wall decreases as they marginate to the RBC-free layer. As expected, platelets approach the wall faster with increasing shear rate. Plotting $\Delta\overline{w}$ as a function of the average distance traveled $\bar{x}$ [Fig. 3(b)] shows that the variation of $\Delta\overline{w}$ as a function of $\bar{x}$ is almost independent of $\dot{\gamma}_w$. This result verifies the scaling relation for margination length introduced in (2). At higher shear rates, the values of $\Delta\overline{w}$ is slightly lower. This effect is likely due to the larger RBC-free layer δ.

The effect of shear rate on margination rate is unclear due to disparities among experimental results from the literature. In rectangular channels with 30, 50, and 100 μm widths, the near-wall platelet concentration was observed above sufficiently large shear rates of 210 s^{-1} and further increases in shear rate increased the near-wall to core concentration ratio [12]. However, the dependence of the near-wall to core concentration ratio was different between the 30-, 50-, and 100-μm channels. The near-wall to core ratio increased

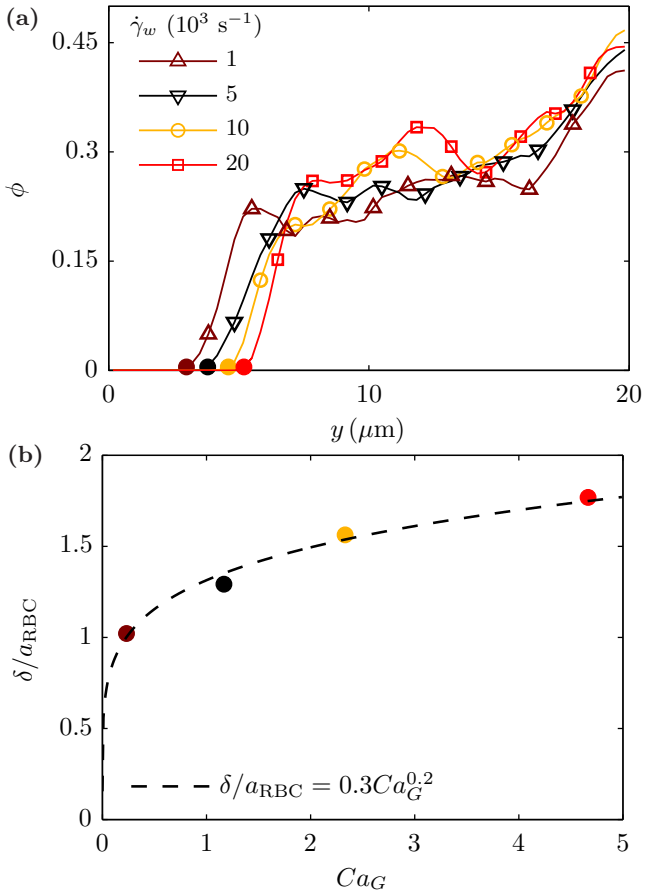

FIG. 2. Effect of wall shear rate on RBC-free layer thickness δ. (a) Profiles of hematocrit ϕ at wall shear rates of $\dot{\gamma}_w = 10^3$, 5×10^3, 10^4, and 2×10^4 s^{-1} in channels of height $H = 40$ μm. Hematocrit profiles are plotted in the cross-channel direction y. The edge of the RBC-free layer is defined as $\phi(\delta) = 0.005$ (denoted by closed circles). (b) The thickness of the RBC-free layer (denoted by closed circles) increases with increasing wall shear rate.

more uniformly at 100 μm compared to 50- and 30-μm channels [12]. The results of Aarts *et al.* [7] also showed a nearly uniform increase in the near-wall to core concentration ratio of platelets with an increase of shear rate from 240 to 1200 s^{-1}. However, this behavior was in contrast with the results of Ref. [16], where in tubes of 200 μm diameter at a hematocrit of 40%, the rate of lateral transport of platelets was found to be less at wall shear rates of 250 or 1220 s^{-1} compared to 560 s^{-1}. The results of Zhao *et al.* [17] showed a small increase of platelet near-wall excess when the shear rate was increased five times from 3000 to 15 000 s^{-1}.

In our analysis for deriving margination length, we assumed that suspensions of deformable RBCs exhibit shear-induced diffusivity with the same functional form as shear-induced diffusivity in suspensions of rigid spheres, i.e., $D_{yy} = K\dot{\gamma}a^2$. In suspensions of rigid spheres, the nondimensional parameter K depends on the hematocrit ϕ. We calculated the RESID of platelets in the cross flow direction from platelet trajectories at various wall shear rates. As expected, RESID of platelets is lowest in the RBC-free region [Fig. 4(a)]. The maximum of $D_{yy}(y)/\dot{\gamma}_w$ occurs at $y \sim 8$ μm, collocated with the first peak

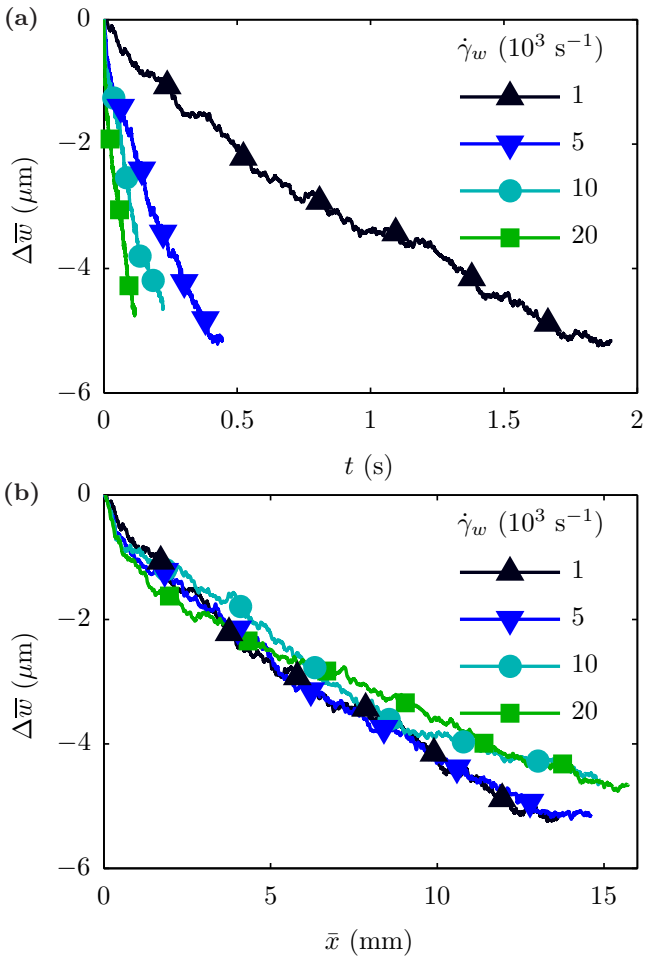

FIG. 3. Average relative distance of platelets from the channel wall at wall shear rates of $\dot{\gamma}_w = 10^3$, 5×10^3, 10^4, and 2×10^4 s^{-1} plotted as a function of (a) time and (b) average distance traveled along the flow direction $\bar{x}$. The channel height is $H = 40$ μm. The average relative distance of platelets from the wall is defined by $\Delta\overline{w}(t) = \overline{w}(t) - \overline{w}(0)$, where $\overline{w}(t)$ denotes the average distance of marginating particles from the wall $\overline{w}(t) = H/2 - |\overline{y(t) - H/2}|$.

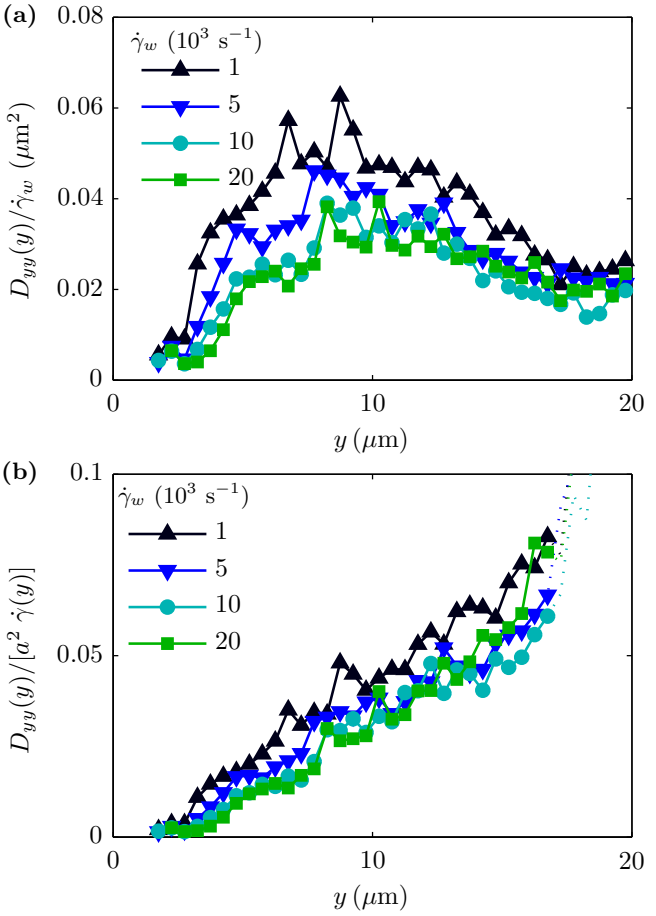

FIG. 4. Cross-channel profiles of platelet effective diffusivity D_{yy} calculated from DNS platelet trajectories at various shear rate rates in channels of height $H = 40$ μm. Effective diffusivity is normalized by (a) wall shear rate $\dot{\gamma}_w$ and (b) by $a^2\dot{\gamma}(y)$, where a is the platelet effective radius and $\dot{\gamma}(y)$ is the local shear rate in the cross flow direction y.

of the hematocrit profile [Fig. 2(a)]. Despite the vanishing (time-averaged) shear rate in the channel center, the value of $D_{yy}/\dot{\gamma}_w$ in the channel center is nonzero. This nonzero value is due to the finite size of RBCs and platelets. Figure 4(b) shows that, similar to suspensions of rigid particles, the nondimensional parameter $K = D_{yy}/\dot{\gamma}a^2$ in RBC suspensions increases with increasing hematocrit ϕ.

In addition to ϕ, the value of K also depends on $\dot{\gamma}$. Figure 4 shows that D_{yy} normalized by shear rate is a weak function of shear rate and the value of K decreases with increasing $\dot{\gamma}_w$. While effective diffusivity of rigid spheres in noncolloidal suspensions scales linearly with $\dot{\gamma}$ [44,47,69], RESID scales sublinearly with $\dot{\gamma}$. The decrease of $D_{yy}/\dot{\gamma}a^2$ with increasing $\dot{\gamma}$ is consistent with the results of numerical studies of Zhao *et al.* [30], who found that the nondimensional self-diffusivity of platelets decreases with Ca in suspensions of platelets and RBCs flowing in microchannels of $H = 34$ μm. Pranay *et al.* [76] found that the nondimensional short-time self-diffusivity $D_{yy}/\dot{\gamma}a^2$ of elastic capsules is a nonmonotonic function of Ca over a range of $0.08 \leqslant \mathrm{Ca} \leqslant 0.6$ with a maximum value of $D_{yy}/\dot{\gamma}a^2$ occurring at $\mathrm{Ca} \approx 0.14$.

B. Effect of channel size

We investigated the effect of channel height H on RBC migration and platelet margination rate by simulating the flow of RBC and platelet suspensions in channels of height $H = 40$, 80, and 160 μm. The RBCs have an effective radius $a_{\mathrm{RBC}} = 2.9$ μm. Simulations were performed at a hematocrit of $\phi = 0.20$. The simulation parameter details are given in Table II. The wall shear rates $\dot{\gamma}_w$ are based on matching RBC shear

TABLE II. DNS parameters of test cases for studying the effect of channel size on margination. In all cases, the channel depth in the z direction is 40 μm and the RBC volume fraction is $\phi = 0.20$.

H (μm)	L (μm)	RBCs	Platelets	$\dot{\gamma}_w$ (s^{-1})	Ca$_G$
40	80	240	100	503	0.28
80	40	240	100	242	0.14
160	40	480	400	100	0.07

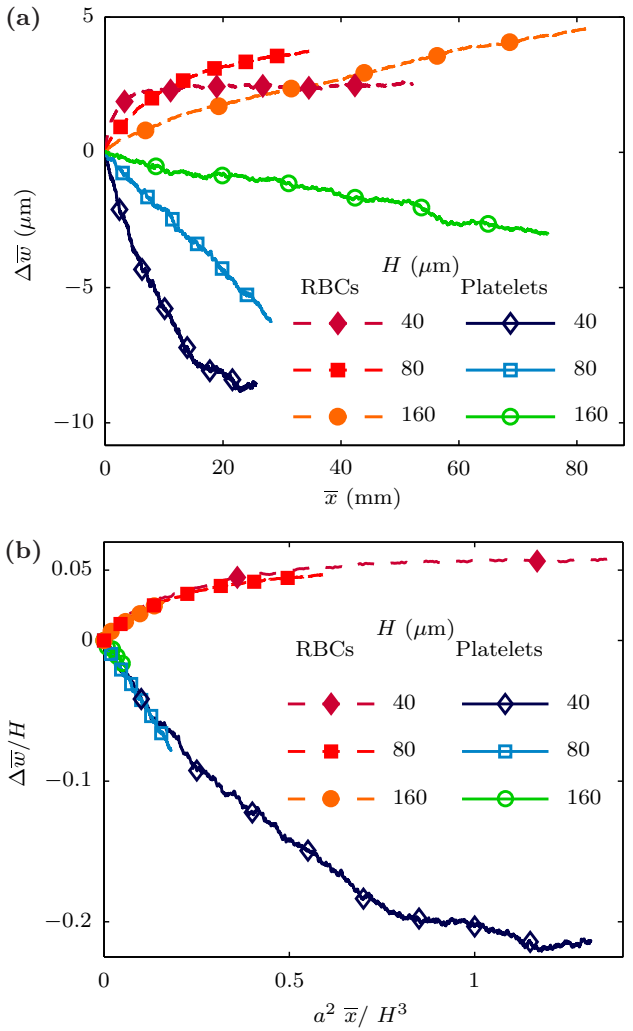

FIG. 5. Effect of channel size H on RBC migration and platelet margination rate. (a) The average relative distance of RBCs and platelets $\Delta\overline{w}$ is plotted as a function of average distance traveled $\overline{w}$ in channels of height $H = 40$, 80, and 160 μm. (b) Normalizing $\Delta\overline{w}$ by channel height H and normalizing $\bar{x}$ by a^2/H^3 results in a collapse of the curves.

capillary number Ca_G. The platelets are modeled as oblate spheroids with a major axis of 2.3 μm and aspect ratio of 2.3.

The average lateral displacement of RBCs and platelets relative to the channel wall $\Delta\overline{w}$ as a function of the average distance traveled $\overline{x}$ for various H values is shown in Fig. 5(a). The margination developing length L_D is much shorter for smaller channels. Also, RBC migration occurs over a much shorter length compared to platelet margination. This large difference in developing scales shows that platelet margination cannot be explained by passive advection of platelets by plasma as RBCs migrate towards the channel center. If $\Delta\overline{w}$ is normalized by height H and $\overline{x}$ is normalized by a^2/H^3, RBC and platelet average trajectories collapse for all cases [Fig. 5(b)]. This result verifies the scaling relation for margination length introduced in (2). Also, when $\overline{x}$ of RBCs and platelets is scaled by the square of their equivalent radii a^2, the development length of RBC migration and platelet margination appears to occur on closer length scales, both of which are of $O(1)$.

In most experimental studies, the concentration of marginating particles is measured at large entrance lengths such that variations in concentration are not detectable. We are not aware of an experimental study specifically designed to measure the effect of channel size on margination developing length, yet a comparison of margination developing length from different studies performed at various channel sizes supports our results that margination development length greatly increases with the increase of channel size. Xu and Wootton [77] found that near-wall platelet concentration in tubes of $D = 3$ mm perfused with whole porcine blood is doubled in steady flow at $L = 50$ cm from the blood reservoir, but only increased by ≈1.5-fold at $L = 10$ cm. While the near-wall platelet concentration is approximately doubled in tubes of $D = 3$ mm over $L = 50$ cm ($L/D \approx 167$), the near-wall concentration of platelet-sized beads is doubled over $L \lesssim 5$ mm in a tube of $D = 200$ μm ($L/D \approx 25$) perfused with a RBC suspension of $\phi = 0.30$ [15]. Zhao *et al.* [17] reported a margination development length of $\lesssim$2.5 mm in 100-μm ($L/H \lesssim 25$) square channels perfused with 40% hematocrit RBC suspensions. They measured a near-wall excess of sevenfold to ninefold at $L = 2.5$ mm in RBC suspensions of $\phi = 0.40$.

C. Effect of particle size and deformability

To identify the particle properties that cause margination, we varied the size or the deformability of a subset of RBCs while keeping the properties of the remaining RBCs unchanged. Then we compare the margination rates of the modified RBCs.

We considered the flow of RBC suspensions in channels of height $H = 40$ μm at a wall shear rate of $\dot{\gamma}_w = 10 \times 10^3$ s^{-1}. The wall shear rate $\dot{\gamma}_w$ is based on the matching channel Reynolds number Re and RBC shear capillary number Ca_G. The RBCs have an effective radius $a_{\mathrm{RBC}} = 2.8$ μm, resulting in a confinement ratio of $2a_{\mathrm{RBC}}/H = 0.14$. A total number of 272 RBCs results in an average hematocrit of $\phi = 0.20$.

The relative size of marginating particles compared to the RBCs is denoted by $r^* = a_m/a_{\mathrm{RBC}}$, where a_m is the effective radius of the marginating particle. We compared the margination rate of rigid RBCs to the margination rate of small soft RBCs and small rigid RBCs. The mechanical properties of the small soft RBCs (i.e., membrane shear modulus G, bending modulus $\tilde{\kappa}$, area constraint coefficient k_a, and volume constraint coefficient k_v) were scaled by matching the nondimensional parameters $\mathrm{Ca}_G = \dot{\gamma} a\mu/G$, $\mathrm{Ca}_\kappa = \dot{\gamma} a^3\mu/\tilde{\kappa}$, $\mathrm{Ca}_a = \dot{\gamma} a\mu/k_a$, and $\mathrm{Ca}_v = \dot{\gamma}\mu/k_v$. The relative deformability of marginating particles compared to the RBCs is denoted by $\mathrm{Ca}^* = \mathrm{Ca}_m/\mathrm{Ca}_{\mathrm{RBC}}$, where Ca_m and $\mathrm{Ca}_{\mathrm{RBC}}$ are any of the above nondimensional parameters (i.e., Ca_G, Ca_κ, etc.). By comparing the dynamics of single RBCs of $r^* = 1$ and 0.5, we have verified that the above scaling of the RBC membrane mechanical properties results in similar dynamics. A total number of 100 small marginating particles is used. To reduce the effect of rigid RBCs on the flow, two simulations with a total number of 50 rigid RBCs were performed for rigid RBCs. The initial locations of RBCs and marginating particles are

TABLE III. Properties of marginating particles in test cases for studying the effect of size and deformability on margination. The domain size is $80 \times 40 \times 40\ \mu\text{m}^3$.

Simulation	Size of marginating particles r^*	Ca^*
small rigid RBCs	0.5	0
small soft RBCs	0.5	1
rigid RBCs	1.0	0

identical in all cases. The properties of marginating particles for different cases are listed in Table III.

Figure 6 shows the average trajectories of RBCs and marginating particles. Smaller size and less deformability both lead to particle margination. A comparison of average trajectories of rigid RBCs with the average trajectories of soft small RBCs shows that rigidity has a more significant effect compared to size within the range of parameters in this study (Fig. 6). When both effects are combined, i.e., small rigid RBCs, the margination rate is the most rapid.

D. Effect of particle shape on margination rate

We studied the effect of shear rate on platelet margination by simulating the flow of RBC and platelet suspensions in channels of height $H = 40\ \mu\text{m}$ at $\dot{\gamma}_w = 10 \times 10^3\ \text{s}^{-1}$. The wall shear rate $\dot{\gamma}_w$ is based on matching channel Reynolds number Re and RBC shear capillary number Ca_G. The RBCs have an effective radius $a_{\text{RBC}} = 2.8\ \mu\text{m}$, resulting in a confinement ratio of $2a_{\text{RBC}}/H = 0.14$. A total number of 272 RBCs results in $\phi = 0.20$. The marginating particles are modeled as rigid spheroids with aspect ratios of $\mathcal{R} = 0.5, 1, 2$, and 4 and volume $V = 8\ \mu\text{m}^3$. A total number of 100 rigid spheroids is used in each simulation. The initial locations of RBCs and spheroids are identical in all cases.

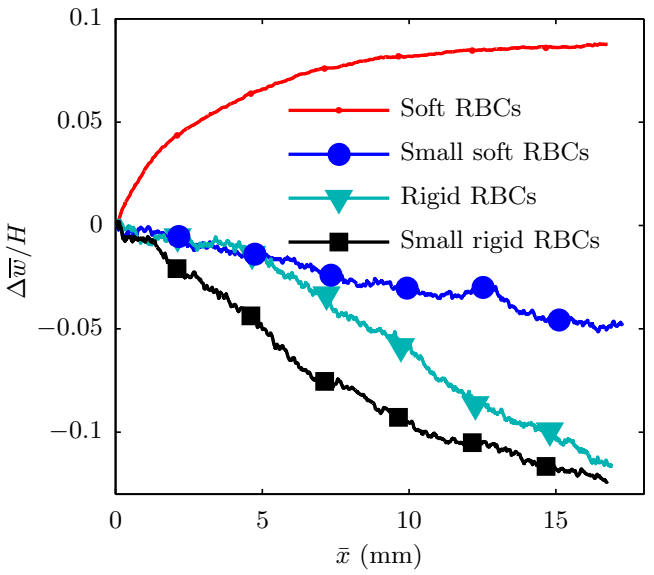

FIG. 6. Average relative distance of platelets of various size and deformability from the channel wall. The channel height is $H = 40\ \mu\text{m}$.

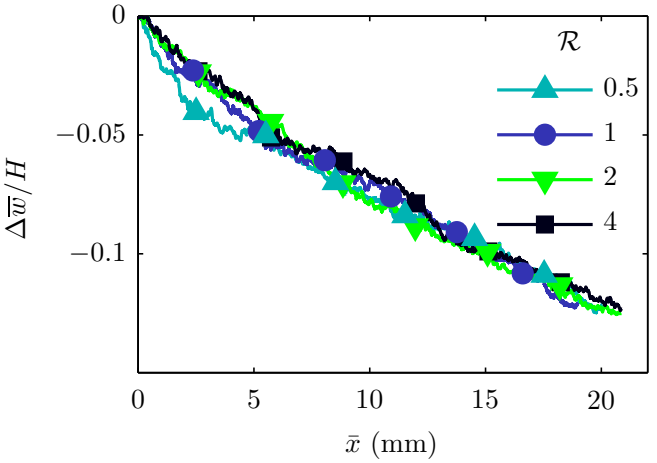

FIG. 7. Average relative distance of platelets of various aspect ratio ($\mathcal{R}$) from the channel wall. The channel height is $H = 40\ \mu\text{m}$.

Figure 7 shows that the margination rate is almost independent of the aspect ratio of the marginating particles within the range of parameters studied here. We have previously found that for larger particles with volume $V = 23.5\ \mu\text{m}^3$, margination rate slightly increases as aspect ratio decreases [36]. This different behavior suggests that below a certain volume fraction, the margination rate is independent of the particle aspect ratio. This result is in agreement with the numerical results of Müller *et al.* [37].

V. CONCLUSION

In this study we investigated the effects of important flow and particle properties on margination of particles in RBC suspensions. We derived a scaling law for margination length based on the assumption that margination is mainly driven by RESID. Based on this scaling law, the margination length increases cubically with channel height H and is independent of shear rate. The results of our DNS of the flow of RBCs and marginating particles in straight channels verified the proposed scaling law for margination length. We also showed that rigidity and size both lead to particle margination, with rigidity having a more significant effect compared to size within the range of parameters in this study. Moreover, we showed that the margination rate is almost independent of the aspect ratio of the marginating particles.

Some limitations of this study are as follows. We assumed that platelets are rigid, since the platelet capillary number is smaller than the RBC capillary number ($\text{Ca}_p \approx 0.09\,\text{Ca}_{\text{RBC}}$) due to its smaller size and larger shear modulus. As suggested in [33,35], the deformability of particles may affect particle migration velocities at small but nonzero Reynolds numbers. Even though in our study $\text{Re}_{\text{platelet}} \leqslant 0.02$, the inertia may affect our results, since we have shown that particle deformability has a strong effect on margination. Also, to stabilize the biconcave shape of the RBCs at low shear rates, we have modeled the RBC membrane with a bending modulus an order of magnitude larger than the experimental consensus values for $\tilde{\kappa}$. The larger value of $\tilde{\kappa}$ slightly decreases the RBC deformability, which may result in underestimated

margination rates. However, we expect this effect to be small, since under moderate deformations, the contribution of bending energy is dominated by the in-plane energy.

ACKNOWLEDGMENTS

This work used the Extreme Science and Engineering Discovery Environment, which was supported by National Science Foundation Grant No. ACI-1053575.

APPENDIX: DERIVATION OF THE SCALING RELATION FOR MARGINATION LENGTH

An estimate of the margination development length L_D can be obtained by a simple analysis of the flow of suspension of RBCs and marginating particles. We follow the analysis of Nott and Brady [44] for estimating the development length of concentration profiles in suspensions of rigid spheres. To obtain a scaling relation for margination length, we consider a suspension of RBCs and marginating particles flowing between two parallel plates with a separation distance of H.

Assuming that RESID governs lateral displacement of particles in the RBC-filled region, we can estimate the average lateral displacement of marginating particles $\Delta\overline{w}$ at time t as

$$\Delta\overline{w} \sim 2\sqrt{\overline{D_{yy}}t}, \tag{A1}$$

where $\overline{D_{yy}}$ is the average coefficient of RBC-enhanced shear-induced diffusivity in the channel. The average relative distance of marginating particles from the wall is defined by $\Delta\overline{w}(t) = \overline{w}(t) - \overline{w}(0)$, where $\overline{w}(t)$ denotes the average distance of marginating particles from the wall $\overline{w}(t) = H/2 - \overline{|y(t) - H/2|}$. Combining (1) and (A1), $\Delta\overline{w}$ at time t is given by

$$\Delta\overline{w} \sim 2\sqrt{K\bar{\dot{\gamma}}a^2 t}, \tag{A2}$$

where $\bar{\dot{\gamma}}$ is the average shear rate across the channel. To express $\Delta\overline{w}$ in terms of the average distance traveled in the flow direction $\bar{x}$ we can write $t = \bar{x}/U$, where U is the average velocity in the flow direction. Assuming that the velocity profile of the suspension in the channel is parabolic everywhere, the average velocity U can be estimated as $U = H\bar{\dot{\gamma}}/3$, yielding $t = 3\bar{x}/H\bar{\dot{\gamma}}$. Substituting this expression in (A2), we can write $\Delta\overline{w}$ as a function of $\bar{x}$,

$$\left(\frac{\Delta\overline{w}}{H}\right)^2 \sim 12K\frac{a^2\bar{x}}{H^3}. \tag{A3}$$

We define the margination development length L_D as the length over which the average relative distance of particles from the wall is $\sim H$, i.e., $L_D = \bar{x}|_{\Delta\overline{w}\sim H}$. Using this and (A3), we can derive an expression for the margination length scale

$$L_D \sim \frac{H^3}{12Ka^2}. \tag{A4}$$

[1] D. M. Husband, L. A. Mondy, E. Ganani, and A. L. Graham, Rheol. Acta **33**, 185 (1994).
[2] G. P. Krishnan, S. Beimfohr, and D. T. Leighton, J. Fluid Mech. **321**, 371 (2006).
[3] M. K. Lyon and L. G. Leal, J. Fluid Mech. **363**, 57 (1998).
[4] D. Semwogerere and E. R. Weeks, Phys. Fluids **20**, 043306 (2008).
[5] H. Mohammadigoushki and J. J. Feng, Phys. Rev. Lett. **109**, 084502 (2012).
[6] H. Mohammadigoushki and J. J. Feng, Langmuir **29**, 1370 (2013).
[7] P. A. M. M. Aarts, S. A. T. van den Broek, G. W. Prins, G. D. C. Kuiken, J. J. Sixma, and R. M. Heethaar, Arteriosclerosis **8**, 819 (1988).
[8] M. R. Beck, Jr. and E. C. Eckstein, Biorheology **17**, 455 (1980).
[9] A. A. Palmer, Bibl. Anat. **9**, 300 (1967).
[10] G. J. Tangelder, D. W. Slaaf, H. C. Tierlinck, R. Alewijnse, and R. S. Reneman, Microvasc. Res. **23**, 214 (1982).
[11] G. J. Tangelder, H. C. Teirlinck, D. W. Slaaf, and R. S. Reneman, Am. J. Physiol.—Heart C. **248**, H318 (1985).
[12] E. C. Eckstein, D. L. Bilsker, C. M. Waters, J. S. Kippenhan, and A. W. Tilles, Ann. NY Acad. Sci. **516**, 442 (1987).
[13] E. C. Eckstein, A. W. Tilles, and F. J. Millero, Microvasc. Res. **36**, 31 (1988).
[14] A. W. Tilles and E. C. Eckstein, Microvasc. Res. **33**, 211 (1987).
[15] C. M. Waters and E. C. Eckstein, Artificial Organs **14**, 7 (1990).
[16] C. Yeh and E. C. Eckstein, Biophys. J. **66**, 1706 (1994).
[17] R. Zhao, M. V. Kameneva, and J. F. Antaki, Biorheology **44**, 161 (2007).
[18] A. Kumar and M. D. Graham, Phys. Rev. E **84**, 066316 (2011).
[19] A. Kumar and M. D. Graham, Soft Matter **8**, 10536 (2012).
[20] A. Kumar and M. D. Graham, Phys. Rev. Lett. **109**, 108102 (2012).
[21] L. L. Munn and M. M. Dupin, Ann. Biomed. Eng. **36**, 534 (2008).
[22] J. C. Firrell and H. H. Lipowsky, Am. J. Physiol.—Heart C. **256**, H1667 (1989).
[23] H. L. Goldsmith and S. Spain, Microvasc. Res. **27**, 204 (1984).
[24] H. W. Hou, A. A. S. Bhagat, A. G. L. Chong, P. Mao, K. S. W. Tan, J. Han, and C. T. Lim, Lab Chip **10**, 2605 (2010).
[25] T. Tanaka, T. Ishikawa, K. Numayama-Tsuruta, Y. Imai, H. Ueno, T. Yoshimoto, N. Matsuki, and T. Yamaguchi, Biomed. Microdev. **14**, 25 (2012).
[26] J. R. Clausen, D. A. Reasor, Jr., and C. K. Aidun, Comput. Phys. Commun. **181**, 1013 (2010).
[27] H. Lei, D. A. Fedosov, B. Caswell, and G. E. Karniadakis, J. Fluid Mech. **722**, 214 (2013).
[28] L. Crowl and A. L. Fogelson, J. Fluid Mech. **676**, 348 (2011).
[29] E. C. Eckstein and F. Belgacem, Biophys. J. **60**, 53 (1991).
[30] H. Zhao, E. S. G. Shaqfeh, and V. Narsimhan, Phys. Fluids **24**, 011902 (2012).
[31] A. Kumar, R. G. Henríquez Rivera, and M. D. Graham, J. Fluid Mech. **738**, 423 (2014).
[32] K. Vahidkhah, S. L. Diamond, and P. Bagchi, Biophys. J. **106**, 2529 (2014).

[33] Y.-L. Chen, RSC Adv. **4**, 17908 (2014).
[34] B. P. Ho and L. G. Leal, J. Fluid Mech. **65**, 365 (1974).
[35] T. Krüger, B. Kaoui, and J. Harting, J. Fluid Mech. **751**, 725 (2014).
[36] D. A. Reasor, Jr., M. Mehrabadi, D. N. Ku, and C. K. Aidun, Ann. Biomed. Eng. **41**, 238 (2013).
[37] K. Müller, D. A. Fedosov, and G. Gompper, Sci. Rep. **4**, 4871 (2014).
[38] S. S. Shevkoplyas, T. Yoshida, L. L. Munn, and M. W. Bitensky, Anal. Chem. **77**, 933 (2005).
[39] P. Charoenphol, S. Mocherla, D. Bouis, K. Namdee, D. J. Pinsky, and O. Eniola-Adefeso, Atherosclerosis **217**, 364 (2011).
[40] P. Charoenphol, P. J. Onyskiw, M. Carrasco-Teja, and O. Eniola-Adefeso, J. Biomech. **45**, 2822 (2012).
[41] J. Tan, A. Thomas, and Y. Liu, Soft Matter **8**, 1934 (2012).
[42] K. Namdee, A. J. Thompson, P. Charoenphol, and O. Eniola-Adefeso, Langmuir **29**, 2530 (2013).
[43] A. J. Thompson, E. M. Mastria, and O. Eniola-Adefeso, Biomaterials **34**, 5863 (2013).
[44] P. R. Nott and J. F. Brady, J. Fluid Mech. **275**, 157 (1994).
[45] E. C. Eckstein, D. G. Bailey, and A. H. Shapiro, J. Fluid Mech. **79**, 191 (1977).
[46] D. Leighton and A. Acrivos, Chem. Eng. Sci. **41**, 1377 (1986).
[47] D. Leighton and A. Acrivos, J. Fluid Mech. **181**, 415 (1987).
[48] D. A. Reasor, Jr., J. R. Clausen, and C. K. Aidun, Int. J. Numer. Methods Fluids **68**, 767 (2012).
[49] R. M. MacMeccan, J. R. Clausen, G. P. Neitzel, and C. K. Aidun, J. Fluid Mech. **618**, 13 (2009).
[50] D. A. Reasor, Jr., J. R. Clausen, and C. K. Aidun, J. Fluid Mech. **726**, 497 (2013).
[51] C. K. Aidun, Y. Lu, and E.-J. Ding, J. Fluid Mech. **373**, 287 (1998).
[52] E.-J. Ding and C. K. Aidun, J. Fluid Mech. **423**, 317 (2000).
[53] S. Chen and G. D. Doolen, Annu. Rev. Fluid Mech. **30**, 329 (1998).
[54] A. J. C. Ladd, J. Fluid Mech. **271**, 285 (1994).
[55] A. J. C. Ladd, J. Fluid Mech. **271**, 311 (1994).
[56] S. Succi, *The Lattice Boltzmann Equation for Fluid Dynamics and Beyond* (Oxford University Press, Oxford, 2001).
[57] C. K. Aidun and J. R. Clausen, Annu. Rev. Fluid Mech. **42**, 439 (2010).
[58] P. Bhatnagar, E. Gross, and M. Krook, Phys. Rev. **94**, 511 (1954).
[59] J. Li, M. Dao, C. T. Lim, and S. Suresh, Biophys. J. **88**, 3707 (2005).
[60] M. Dao, J. Li, and S. Suresh, Mater. Sci. Eng. C **26**, 1232 (2006).
[61] I. V. Pivkin and G. E. Karniadakis, Phys. Rev. Lett. **101**, 118105 (2008).
[62] D. A. Fedosov, B. Caswell, and G. Karniadakis, Biophys. J. **98**, 2215 (2010).
[63] D. A. Fedosov, B. Caswell, and G. E. Karniadakis, Comput. Methods Appl. Mech. Eng. **199**, 1937 (2010).
[64] J. F. Marko and E. D. Siggia, Macromolecules **28**, 8759 (1995).
[65] C. Bustamante, Z. Bryant, and S. B. Smith, Nature (London) **421**, 423 (2003).
[66] D. A. Fedosov, Multiscale modeling of blood flow and soft matter, Ph.D. thesis, Brown University, 2010.
[67] J. Lidmar, L. Mirny, and D. R. Nelson, Phys. Rev. E **68**, 051910 (2003).
[68] J. R. Clausen, D. A. Reasor, and C. K. Aidun, J. Fluid Mech. **685**, 202 (2011).
[69] A. Sierou and J. F. Brady, J. Fluid Mech. **506**, 285 (2004).
[70] H. Byun, T. R. Hillman, J. M. Higgins, M. Diez-Silva, Z. Peng, M. Dao, R. R. Dasari, S. Suresh, and Y. Park, Acta Biomater. **8**, 4130 (2012).
[71] E. D. Gilmore, C. Hudson, D. Preiss, and J. Fisher, Am. J. Physiol.—Heart C. **288**, H2912 (2005).
[72] G. S. Kurland and S. E. Charm, *Blood Flow and Microcirculation* (Wiley, New York, 1974).
[73] H. H. Lipowsky, S. Kovalcheck, and B. W. Zweifach, Circ. Res. **43**, 738 (1978).
[74] S. Singhal, R. Henderson, K. Horsfield, K. Harding, and G. Cumming, Circ. Res. **33**, 190 (1973).
[75] M. V. Kameneva, Z. J. Wu, A. Uraysh, B. Repko, K. N. Litwak, T. R. Billiar, M. P. Fink, R. L. Simmons, B. P. Griffith, and H. S. Borovetz, Biorheology **41**, 53 (2004).
[76] P. Pranay, R. G. Henríquez-Rivera, M. D. Graham, and R. G. Henriquez-Rivera, Phys. Fluids **24**, 061902 (2012).
[77] C. Xu and D. M. Wootton, Biorheology **41**, 113 (2004).